

# Kalman inversion stress microscopy

V. Nier<sup>1</sup>, G. Peyret<sup>2</sup>, J. d’Alessandro<sup>2</sup>, S. Ishihara<sup>4</sup>, B. Ladoux<sup>2,3</sup> and P. Marcq<sup>1,\*</sup>

**1** Laboratoire Physico Chimie Curie, Institut Curie, PSL Research University, Sorbonne Université, CNRS, 26 rue d’Ulm, 75005 Paris, France

**2** Institut Jacques Monod, CNRS, Université Paris Diderot, 75013 Paris, France

**3** Mechanobiology Institute, National University of Singapore, Singapore

**4** Graduate School of Arts and Sciences, The University of Tokyo, Tokyo 153-8902, Japan

\* Corresponding author, philippe.marcq@curie.fr

August 29, 2018

## Abstract

Although mechanical cues are crucial to tissue morphogenesis and development, the tissue mechanical stress field remains poorly characterized. Given traction force timelapse movies, as obtained by traction force microscopy of *in vitro* cellular sheets, we show that the tissue stress field can be estimated by Kalman filtering. After validation using numerical data, we apply Kalman inversion stress microscopy to experimental data. We combine the inferred stress field with velocity and cell shape measurements to quantify the rheology of epithelial cell monolayers in physiological conditions, found to be close to that of an elastic and active material.

## Introduction

The last decades have led to a growing awareness of the importance of mechanotransduction in cell and developmental biology<sup>1,2</sup>. Noteworthy examples include the cell fate determination of stem cells as a function of their microenvironment<sup>3</sup>, or the force-sensing machinery present at adherens junctions<sup>4</sup>. Despite much recent effort<sup>5</sup>, the measurement of internal forces in tissues remains challenging, and is often limited to relative force estimates, as is the case for tissue scale ablation<sup>6</sup> or geometry-based inference<sup>7</sup>. Traction force microscopy (TFM), a well established tool of mechanobiology, allows to estimate *in vitro* the force field exerted by cells and cell assemblies on their environment<sup>8,9</sup>. Since internal stresses and external forces are balanced, a seemingly natural way to obtain the stress field from the traction force field would be to invert the force balance equation. This equation is however not invertible, since three unknowns, the components of the symmetric stress tensor, must be deduced from the two linear equations that correspond to the two components of the traction force. The problem may become invertible at

the cost of postulating a tissue rheology<sup>10</sup>: Monolayer Stress Microscopy (MSM) relies on the assumption of an elastic tissue rheology, which is disputable given various evidence for viscous<sup>11</sup>, plastic<sup>12</sup> and active<sup>13</sup> behaviour in tissues. Recently, we have described, validated<sup>14</sup>, and applied<sup>13</sup> Bayesian inversion stress microscopy (BISM), a stress inference method that dispenses with rheological hypotheses yet allows to estimate the absolute value of the internal stress field of a cell sheet from an image of traction force measurement. In a Bayesian framework, the inferred stress is the mode of the posterior probability distribution function (pdf), given a prior stress distribution function equivalent to a regularizing term that controls the norm of the stress.

Since TFM yields time-lapse movies that allowed to follow the time evolution of the traction force field, we adapt Kalman filtering<sup>15</sup> to this inversion problem<sup>16</sup>, and formulate Kalman inversion stress microscopy (KISM). The Kalman filter is, in a mean square error sense, an optimal estimator for Gaussian statistical models and remains the best linear estimator in the non-Gaussian case<sup>17</sup>. Qualitatively, correlations between successive data frames are preserved for high enough time resolution. Kalman filtering exploits this feature to obtain an estimate of the state variable while solving an under-determined inversion problem. Since KISM is free from any assumption concerning tissue mechanics, we use the inferred stress field to study epithelial rheology.

## Materials and methods

### Statistical model

Neglecting inertia, the force balance equation of a planar cell sheet exchanging momentum with its substrate reads:

$$\operatorname{div} \sigma = \vec{f}, \quad (1)$$

where  $\sigma(\vec{r}, t)$  and  $\vec{f}(\vec{r}, t)$  respectively denote the two-dimensional, symmetric stress tensor and traction force fields at position  $\vec{r}$  and time  $t$ . On a discrete cartesian grid with spatial resolution  $l$ , we denote  $\nabla$  the discretized divergence (matrix) operator, computed with fourth-order centered finite differences. Using the acquisition time as the time unit,  $t$  becomes a discrete variable,  $t = 1, \dots, T$ , where  $T$  is the total number of frames. At each time step  $t$ , Eq. (1) translates into a system of coupled linear equations, where the unknown quantities are the stress field components  $\sigma_{xx}(i, j, t)$ ,  $\sigma_{yy}(i, j, t)$  and  $\sigma_{xy}(i, j, t)$ , with  $i = 1, \dots, N_x$ ,  $j = 1, \dots, N_y$ , using on a grid of size  $N_x N_y$ . For each point of coordinates  $(i, j)$  on the spatial grid, solving this system amounts to determining three unknowns given two equations, one for each component of the traction force field  $f_x(i, j, t)$  and  $f_y(i, j, t)$ : the system is not invertible, and calls for non-algebraic methods for its solution.

We perform Kalman inversion<sup>16</sup>, and accordingly probabilize the problem. Let  $\vec{F}^t$  be the traction force vector encompassing both traction force components on the whole spatial domain at time  $t$ :

$$\vec{F}^t = [f_x(1, 1, t) \cdots f_x(N_x, N_y, t) f_y(1, 1, t) \cdots f_y(N_x, N_y, t)]^T, \quad (2)$$

where the superscript  $T$  denotes the transpose. Let  $\vec{\sigma}^t$  be a similar stress *vector* including the three stress components at all grid points at time  $t$ :

$$\vec{\sigma}^t = [\sigma_{xx}(1, 1, t) \dots \sigma_{xx}(N_x, N_y, t) \sigma_{yy}(1, 1, t) \dots \sigma_{yy}(N_x, N_y, t) \sigma_{xy}(1, 1, t) \dots \sigma_{xy}(N_x, N_y, t)]^T. \quad (3)$$

The observation model reads:

$$\nabla \vec{\sigma}^t = \vec{F}^t + \vec{\phi}^t \quad (4)$$

with an additive, zero-mean, Gaussian observation noise  $\vec{\phi}^t \sim \mathcal{N}(\vec{0}, s^2 I)$  of variance  $s^2$ , with correlations  $\langle \phi_\alpha^t \phi_\beta^{t'} \rangle = s^2 \delta_{\alpha\beta} \delta_{tt'}$  for all components  $\alpha, \beta = 1, \dots, 2N_x N_y$ . The simplest possible expression of an evolution model for the stress field is a random walk:

$$\vec{\sigma}^t = I \vec{\sigma}^{t-1} + \vec{\xi}^t \quad (5)$$

where  $I$  is the identity matrix, and the evolution noise  $\vec{\xi}^t$  is zero-mean, Gaussian with variance  $\gamma^2$ ,  $\vec{\xi}^t \sim \mathcal{N}(\vec{0}, \gamma^2 I)$ , and correlations  $\langle \xi_\alpha^t \xi_\beta^{t'} \rangle = \gamma^2 \delta_{\alpha\beta} \delta_{tt'}$ ,  $\forall \alpha, \beta = 1, \dots, 3N_x N_y$ . In practice we implement the relevant stress-free boundary conditions in the evolution model, introducing an evolution matrix  $B$ :

$$\vec{\sigma}^t = B \vec{\sigma}^{t-1} + \vec{\xi}^t. \quad (6)$$

The matrix  $B$  is equal to the identity matrix  $I$ , except for diagonal components set to zero due to stress-free boundary conditions. In a confined system, we thus set  $\sigma_{ij} n_j = 0$  at the boundary, up to the addition of the evolution noise, where  $\vec{n}$  denotes the vector normal to the edge, and summation over repeated indices is implied.

At time  $t = 1$ , the stress vector and its covariance matrix are respectively initialized as  $\hat{\vec{\sigma}}^1$  and  $S^1$ , as defined below. At times  $t > 1$ , we combine traction force data  $\vec{F}^t$  with the previous stress estimate  $\hat{\vec{\sigma}}^{t-1}$  to compute iteratively  $\hat{\vec{\sigma}}^t$ , the filtered stress at time  $t$ , with the matrix operations<sup>17</sup>:

$$K^t = (BS^{t-1}B^T + \gamma^2 I) \nabla^T (\nabla (BS^{t-1}B^T + \gamma^2 I) \nabla^T + s^2 I)^{-1} \quad (7)$$

$$S^t = (I - K^t \nabla) (BS^{t-1}B^T + \gamma^2 I) (I - K^t \nabla)^T + s^2 K^t (K^t)^T \quad (8)$$

$$\hat{\vec{\sigma}}^t = B \hat{\vec{\sigma}}^{t-1} + K^t (\vec{F}^t - \nabla B \hat{\vec{\sigma}}^{t-1}) \quad (9)$$

where  $K^t$  is the Kalman matrix at time  $t$ . The covariance matrix  $S^t$  allows to determine error bars on the stress estimate  $\hat{\vec{\sigma}}^t$ .

In physical terms, Eqs. (4) and (6) may be interpreted as follows<sup>16</sup>. Let us denote  $\mathcal{F}^t = \{\vec{F}^1, \dots, \vec{F}^t\}$  the set of all traction force data up to time  $t$ . The goal of Kalman filtering is to determine the conditional pdf  $P(\vec{\sigma}^t | \mathcal{F}^t)$ . In the case of Gaussian statistics, this amounts to calculating its mean  $\hat{\vec{\sigma}}^t$  and its covariance matrix  $S^t$ . One iteration step can be decomposed into a prediction step, followed by an update step. The prediction step uses a Chapman-Kolmogorov equation to compute  $P(\vec{\sigma}^t | \mathcal{F}^{t-1})$  given  $P(\vec{\sigma}^{t-1} | \mathcal{F}^{t-1})$  and a (Gaussian) Markov transition kernel  $P(\vec{\sigma}^t | \vec{\sigma}^{t-1})$ , determined by the evolution equation (6):

$$P(\vec{\sigma}^t | \mathcal{F}^{t-1}) = \int d\vec{\sigma}^{t-1} P(\vec{\sigma}^t | \vec{\sigma}^{t-1}) P(\vec{\sigma}^{t-1} | \mathcal{F}^{t-1}). \quad (10)$$

The update step next deduces  $P(\vec{\sigma}^t|\mathcal{F}^t)$  from Bayes formula:

$$P(\vec{\sigma}^t|\mathcal{F}^t) = \frac{P(\vec{F}^t|\vec{\sigma}^t) P(\vec{\sigma}^t|\mathcal{F}^{t-1})}{P(\vec{F}^t|\mathcal{F}^{t-1})}, \quad (11)$$

where  $P(\vec{\sigma}^t|\mathcal{F}^{t-1})$  plays the role of a prior,  $P(\vec{F}^t|\vec{\sigma}^t)$  is the likelihood determined by the observation equation (4), and the denominator is a normalization factor  $P(\vec{F}^t|\mathcal{F}^{t-1}) = \int d\vec{\sigma}^t P(\vec{F}^t|\vec{\sigma}^t) P(\vec{\sigma}^t|\mathcal{F}^{t-1})$ . In the Gaussian case, Eqs. (10-11) lead to the iteration rule (7-9)<sup>16</sup>. For an intuitive derivation of Eqs. (7-8) in a simple, scalar case, we refer the reader to<sup>18</sup>.

Concerning the algorithm's parameters, the observation noise variance  $s^2$  is given by  $s_{\text{exp}}^2$ , the experimental uncertainty on the traction force data. The evolution noise variance  $\gamma^2$  is evaluated from data as follows. Applying  $\nabla$  to (5) and substituting  $\nabla\sigma^t$  using (4), we obtain the evolution equation of the traction force:  $\vec{F}^t = \vec{F}^{t-1} + \vec{\psi}^t$  where  $\vec{\psi}^t = \nabla\vec{\xi}^t + \phi^{t-1} - \phi^t$ , the sum of zero-mean Gaussian noises, is also a zero-mean Gaussian noise. Using the statistical independence in space and time between the different noises, we estimate the order of magnitude of the evolution noise variance:

$$\gamma^2 \approx l^2 \langle\langle (\vec{F}^t - \vec{F}^{t-1})^2 \rangle\rangle + 4l^2 s^2 \quad (12)$$

where  $\langle\langle \dots \rangle\rangle$  denotes spatial and temporal averaging. When inferring the stress field from experimental data, we typically use<sup>14</sup>  $s^2 = s_{\text{exp}}^2 \approx 100 \text{ Pa}^2$  and find  $\gamma^2 \approx 2 \cdot 10^5 \text{ Pa}^2 \mu\text{m}^2$  (HaCaT cells),  $\gamma^2 \approx 3 \cdot 10^4 \text{ Pa}^2 \mu\text{m}^2$  (MDCK cells) when  $l = \lambda = 25 \mu\text{m}$ . For simplicity, we use as initial conditions  $\hat{\sigma}_\alpha^1 = \gamma$ ,  $\forall \alpha$ , and  $S^1 = \gamma^2 I$ .

## Measures of accuracy

At each time step, KISM computes a set  $\{\sigma^{\text{inf}}\}$  of inferred stresses from the set of experimental traction forces  $\{f^{\text{exp}}\}$ . We calculate the inferred traction force field  $\{f^{\text{inf}}\}$  by applying the divergence operator to the inferred stress field:  $\vec{F}^{\text{inf}} = \nabla\vec{\sigma}^{\text{inf}}$ . For each component  $f_i = f_x, f_y$  of  $\vec{f}$ , we calculate the coefficient of determination:

$$R_i^2(t) = 1 - \frac{\sum (f_i^{\text{exp}}(t) - f_i^{\text{inf}}(t))^2}{\sum (f_i^{\text{exp}}(t) - \langle f_i^{\text{exp}}(t) \rangle)^2}. \quad (13)$$

where the sums and the averages  $\langle \dots \rangle$  are performed over space. An aggregate quantifier  $R_f^2$  of the accuracy of inference for a given traction force movie is obtained by averaging  $R_i^2(t)$  over time and over the components  $x$  and  $y$ , with the most accurate estimate corresponding to numerical values of  $R_f^2$  closest to 1. The same measure of accuracy can be defined for numerical data, replacing  $\{f^{\text{exp}}\}$  by  $\{f^{\text{num}}\}$  in the above expression.

Exact, spatially-averaged values of stress components can be calculated directly from traction force data in confined domains where the boundary condition  $\sigma_{ij} n_j = 0$  applies. Denoting as above spatial averages by brackets  $\langle \dots \rangle$ , we have  $\langle \sigma_{ij} \rangle = -\langle f_i x_j \rangle$ <sup>19</sup>, with Cartesian coordinates  $(x_1, x_2) = (x, y)$  (see also<sup>14</sup> for an explicit derivation). Using this relation, we checked that the average inferred stress values  $\langle \sigma_{ij}^{\text{inf}} \rangle$  agree with the values  $\langle \sigma_{ij}^{\text{exp}} \rangle$  computed directly from the traction force data.

## Numerical simulation

For definiteness, we use the simulated traction force field of a compressible viscous tissue, obeying the constitutive equation:

$$\sigma = \eta \left( \vec{\nabla} \vec{v} + \left( \vec{\nabla} \vec{v} \right)^t \right) + \eta' \left( \vec{\nabla} \cdot \vec{v} \right) I, \quad (14)$$

with shear and bulk viscosities  $\eta$  and  $\eta'$ , interacting with its substrate through an effective fluid friction force (friction coefficient  $\xi_d$ ), and driven by  $n_d$  moving, active force dipoles:

$$\text{div } \sigma = \vec{f} = \xi_d \vec{v} - \sum_{n=1}^{n_d} \nabla \cdot p^n(\vec{x}, t). \quad (15)$$

The dipole amplitudes increase towards the boundaries: they are set proportional to  $1+r/l_p$ , where  $r$  is the distance to the center of the domain and  $l_p = 5 \mu\text{m}$  is a penetration length<sup>20</sup>.

The dynamics stems from the actively moving dipoles. Following<sup>21</sup>, we stipulate that the force dipoles tend to align their direction with their velocity, with the following relaxation equation of the orientation  $\theta_d^n$  of the dipole towards the orientation  $\theta_v^n$  of its velocity  $\vec{v}^n$ ,

$$\frac{d\theta_d^n}{dt} = -\frac{1}{\tau_d} (\theta_d^n - \theta_v^n) \quad (16)$$

with a relaxation time  $\tau_d$ . In addition, each dipole velocity  $\vec{v}^n$  is given as an Ornstein-Uhlenbeck process

$$\frac{d\vec{v}^n}{dt} = -\frac{1}{\tau_d} \vec{v}^n + \vec{\varphi}^n \quad (17)$$

with correlation time  $\tau_d$ , and zero-mean, Gaussian white noise  $\vec{\varphi}^n$  with correlations  $\langle \varphi_i^n(t) \varphi_j^n(t') \rangle = s_v^2 \delta_{ij} \delta(t-t')$  for components  $i, j$ . Eqs. (16-17) determine the trajectories of dipoles, starting from random initial positions and orientations. The numerical resolution of Eqs. (14-17) is performed with **FreeFem++**<sup>22</sup>.

We use material parameter values typical of epithelial cell monolayers<sup>14, 20, 21</sup>: friction coefficient  $\xi_d = 10^0 \text{ kPa } \mu\text{m}^{-1}\text{s}$ , shear viscosity  $\eta = 10^4 \text{ kPa } \mu\text{m s}$ , bulk viscosity  $\eta' = \eta$ ,  $n_d = 100$  dipoles with a typical amplitude 1 kPa, a correlation time  $\tau_d = 10^4 \text{ s}$ , a noise amplitude  $s_v = 7 \cdot 10^{-4} \mu\text{m s}^{-3/2}$ . The simulated tissue is confined in a square of area  $100 \times 100 \mu\text{m}^2$ , with a spatial resolution of  $l = 2 \mu\text{m}$ . We include movies of this simulation for the traction force (in kPa) and for the stress (in kPa  $\mu\text{m}$ ) over a total duration of 3 h and with a time step of 30 s (see Movies S1 and S2).

The numerical resolution of the set of equations given above immediately yields a numerical data set of stresses  $\{\sigma^{\text{num}}\}$ . To account for the measurement error, we add to the simulated traction force field a zero-mean, Gaussian white noise of amplitude  $s_{\text{exp}}^{\%} f_{\text{max}}$ , where  $f_{\text{max}}$  is the maximal value of the norm of the traction force, and obtain a numerical data set  $\{f^{\text{num}}\}$  of traction forces. The set  $\{\sigma^{\text{inf}}\}$  of inferred stresses is next

computed from  $\{f^{\text{num}}\}$  with KISM. At time  $t$ , we calculate for each component of the stress  $\sigma_{ij} = \sigma_{xx}, \sigma_{yy}, \sigma_{xy}$  the coefficient of determination

$$R_{ij}^2(t) = 1 - \frac{\sum(\sigma_{ij}^{\text{num}}(t) - \sigma_{ij}^{\text{inf}}(t))^2}{\sum(\sigma_{ij}^{\text{num}}(t) - \langle \sigma_{ij}^{\text{num}}(t) \rangle)^2} \quad (18)$$

An aggregate quantifier  $R_\sigma^2$  of the accuracy of inference is obtained by averaging first over the stress components  $xx$ ,  $yy$  and  $xy$  at time  $t$  (coefficient of determination  $R_\sigma^2(t)$ ), and then over time. As above, the evolution noise variance is computed from averaged traction force increments (Eq. (12)), with typical values  $\gamma^2 \approx 10^5 \text{ Pa}^2 \mu\text{m}^2$  and we use as initial conditions  $\hat{\sigma}_\alpha^1 = \gamma$ ,  $\forall \alpha$ , and  $S^1 = \gamma^2 I$ .

The Kalman inversion that yielded stresses in Movie S2 from the traction force data in Movie S1 required 150 min of Intel-Xeon E5 CPU. As the main computational bottleneck of the algorithm are matrix inversions in (7), we expect the computational cost to scale as  $O(N^3)$ <sup>23</sup>.

## Experimental methods

Cells were cultured in Dulbecco's Modified Eagle Medium, supplemented with 10% of fetal veal serum and 1% of penicillin-streptomycin at 37°C, with 5% CO<sub>2</sub>. For experiments, cells were concentrated at around 4 million cells per mL and a drop of 200  $\mu\text{L}$  was added in the medium of the experimental Petri dish. Incubation time lasted from 15 to 30 min depending on the concentration needed at the beginning of the experiment and on the cell line. Cells that did not attach were then washed and the substrate incubated overnight. Cells were confined in a  $500 \times 500 \mu\text{m}^2$  square domain. The height of the monolayer was of the order of  $h_{\text{HaCaT}} \simeq 3 \mu\text{m}$  and  $h_{\text{MDCK}} \simeq 5 \mu\text{m}$ <sup>14</sup> for HaCaT and MDCK cells, respectively.

To confine the cells to square patterns, we used micro-contact printing on soft gel, as previously described<sup>24</sup>. Briefly, PDMS stamps exhibiting square features were incubated with a fibronectin solution at  $75 \text{ mg mL}^{-1}$  for 45 min. After rinsing with water, the dried stamp was put in contact with the surface of a polyvinyl-alcohol membrane (Sigma Aldrich). Then the membrane was put upside-down on the soft gel to allow the transfer of the protein from the membrane to the gel. Finally, the membrane was dissolved with a 2% Pluronic-F27 (Sigma Aldrich) solution which was let to incubate for 2 h to make the non-printed areas anti-adhesive for the cells.

Live imaging was performed with a 10X objective on a BioStation IM-Q (Nikon) at 37°C and 5% CO<sub>2</sub> with humidification. Images of the cells were taken every 10 min. The velocity fields were calculated by Particle Image Velocimetry (PIV) analysis with MATPIV 1.6.1, a Matlab (the Mathworks) implemented script. An interrogation window of 64 pixels (approximately 41  $\mu\text{m}$ ) was selected with an overlap of 75%. Vectors higher than a speed threshold manually determined were removed, and a local median filter was applied.

Moving epithelial cells exerted traction forces on their substrate that can be calculated from the displacement field of the substrate. This was achieved using 200 nm fluorescent

beads attached on the surface as previously described<sup>13,25</sup>. A Z-stack of images was taken every 10 min. Images were first processed with ImageJ to obtain the best focus plane for each time point (Stack Focuser plugin), then stabilized (Image Stabilizer plugin), and background beads were removed. The substrate displacements were measured with PIV, using interrogation areas of  $15.5 \times 15.5 \mu\text{m}^2$  with an overlap of 75%. Images of fluorescent beads were acquired and compared with an image of the gel at rest, obtained at the end of the experiment. A drop of  $200 \mu\text{L}$  of sodium dodecyl sulfate ( $0.1 \text{ g mL}^{-1}$ ) was added in order to lyse and detach the cells. Forces were calculated from the displacement field by Fourier Transform Traction Cytometry (FTTC) with an open-source ImageJ plugin developed by Qingzong Tseng<sup>26</sup>. The gel had a Young modulus of 15 kPa, with a Poisson ratio of 0.5. We used a regularization parameter of  $10^{-10}$  for FTTC. The gel thickness ( $\approx 200 \mu\text{m}$ ) was large compared to the typical correlation lengths of both the beads' displacements ( $\approx 85 \mu\text{m}$ ) and the traction forces ( $\approx 14 \mu\text{m}$ ), so that finite thickness corrections to the TFM could be safely neglected.

To obtain the cell shape tensor  $Q$  in a cell sheet, we followed the same procedure as described in<sup>13</sup>. A clear image was obtained, with individual cell boundaries visible. The image was smoothed using Bandpass Filter in ImageJ to remove unnecessary details. The filter size of small structures was set to roughly one-third the size of a single cell. The ImageJ plugin OrientationJ was used to detect the direction of the largest eigenvector of the structure tensor of the image<sup>27</sup> for each pixel (for a window size of roughly one-quarter the size of a single cell). The output is the orientation angle  $\theta_Q$  with values ranging from  $-90^\circ$  to  $+90^\circ$ . The local cell shape tensor,  $Q$ , was calculated for each point on a grid that discretized the image, using an in-house Matlab code, averaging over pixel directions in a fixed-size region that contained 3-5 cells:

$$Q = \left\langle \begin{pmatrix} \cos^2 \theta_Q - 1/2 & \cos \theta_Q \sin \theta_Q \\ \cos \theta_Q \sin \theta_Q & \sin^2 \theta_Q - 1/2 \end{pmatrix} \right\rangle, \quad (19)$$

where the brackets denote averaging over a 64 pixels-wide window, with 75% overlap. Only pixels that resided in the region of the cell body were taken into account for this calculation (white regions obtained by Auto Local Threshold function in ImageJ) as cell boundary regions could have orientations that are perpendicular to the cell body.

## Data analysis

All fields were interpolated on the TFM grid using Matlab's `interp2` function, and coarse-grained over boxes of linear extension  $\lambda = 25 \mu\text{m}$ , excluding a domain of width  $\lambda$  along each boundary. We checked that results of the rheological analysis did not change for a larger coarse-graining scale  $\lambda = 50 \mu\text{m}$ . Since the solution first needs to relax to its optimum (Figs. 1, 2 and 3), stress estimates at short time may be unreliable. For this reason, we conservatively discarded the first 10 h of the estimated stress when estimating rheological parameters.

Tensors were decomposed into the sum of a deviatoric (traceless) term and of an isotropic term, as in  $\sigma = \text{dev } \sigma + \frac{1}{2} \text{tr } \sigma I$ , where `tr` denoted the trace (*i.e.*  $\text{tr } \sigma = \sigma_{xx} + \sigma_{yy}$ ).

The symmetrized velocity gradient tensor  $D$  was defined as:

$$D = \begin{pmatrix} \partial_x v_x & \frac{1}{2} (\partial_x v_y + \partial_y v_x) \\ \frac{1}{2} (\partial_x v_y + \partial_y v_x) & \partial_y v_y \end{pmatrix}. \quad (20)$$

Spatial derivatives were computed with Matlab's gradient function on the scale  $\lambda$ . Time derivatives denoted with a dot were total derivatives, as in:

$$\dot{\sigma}_{xx} = \left( \frac{\partial}{\partial t} + \vec{v} \cdot \vec{\nabla} \right) \sigma_{xx}. \quad (21)$$

To quantify plithotactic behavior, we estimated the angles  $\theta_{\sigma v}$  between the direction of the velocity field and the principal axis of the stress tensor  $\sigma$ ; and  $\theta_{\sigma Q}$  between the principal axes of  $\sigma$  and  $Q$ . Following Ref.<sup>10</sup>, we computed angular distributions corresponding to the highest quintile of the stress anisotropy. Relaxing this thresholding condition did not change our results qualitatively, but increased the dispersion and made angular distributions wider. Angular distributions were fitted by a zero-mean von Mises distribution of parameter  $\kappa \geq 0$ :

$$p_{\text{von Mises}}(\theta) = \frac{e^{\kappa \cos 2\theta}}{2\pi I_0(\kappa)} \quad (22)$$

where  $\theta$  belonged to the interval  $[-\frac{\pi}{2}, \frac{\pi}{2}]$  and  $I_0$  denoted the modified Bessel function of order zero. A smaller value of  $\kappa$  corresponds to a wider distribution<sup>28</sup>, which is uniform when  $\kappa = 0$ .

## Results

The state and observation variables of the Kalman filter were defined as the two-dimensional stress and traction force fields  $\sigma(\vec{r}, t)$  (in kPa  $\mu\text{m}$ ) and  $\vec{f}(\vec{r}, t)$  (in kPa), where  $\vec{r}$  and  $t$  denoted position and time (Materials and methods, Statistical model). The observation equation (Eq. (4)) was the linear, two-dimensional force balance equation,  $\text{div } \sigma = \vec{f}$ , discretized on a grid of finite mesh, and supplemented with an additive observation noise, assumed to be Gaussian and white. With applications to confined cellular sheets in mind, the stress-free boundary conditions were implemented in the evolution equation, where the stress fields at two consecutive time steps differed by an additive evolution noise, also Gaussian and white (Eq. (6)). The stress estimate was iteratively updated as an optimal combination of its estimate at the previous time step with the contribution of traction force data at the current time step (Eqs. (7-9)). We emphasize that, contrary to Bayesian inversion, Kalman inversion did not require a prior.

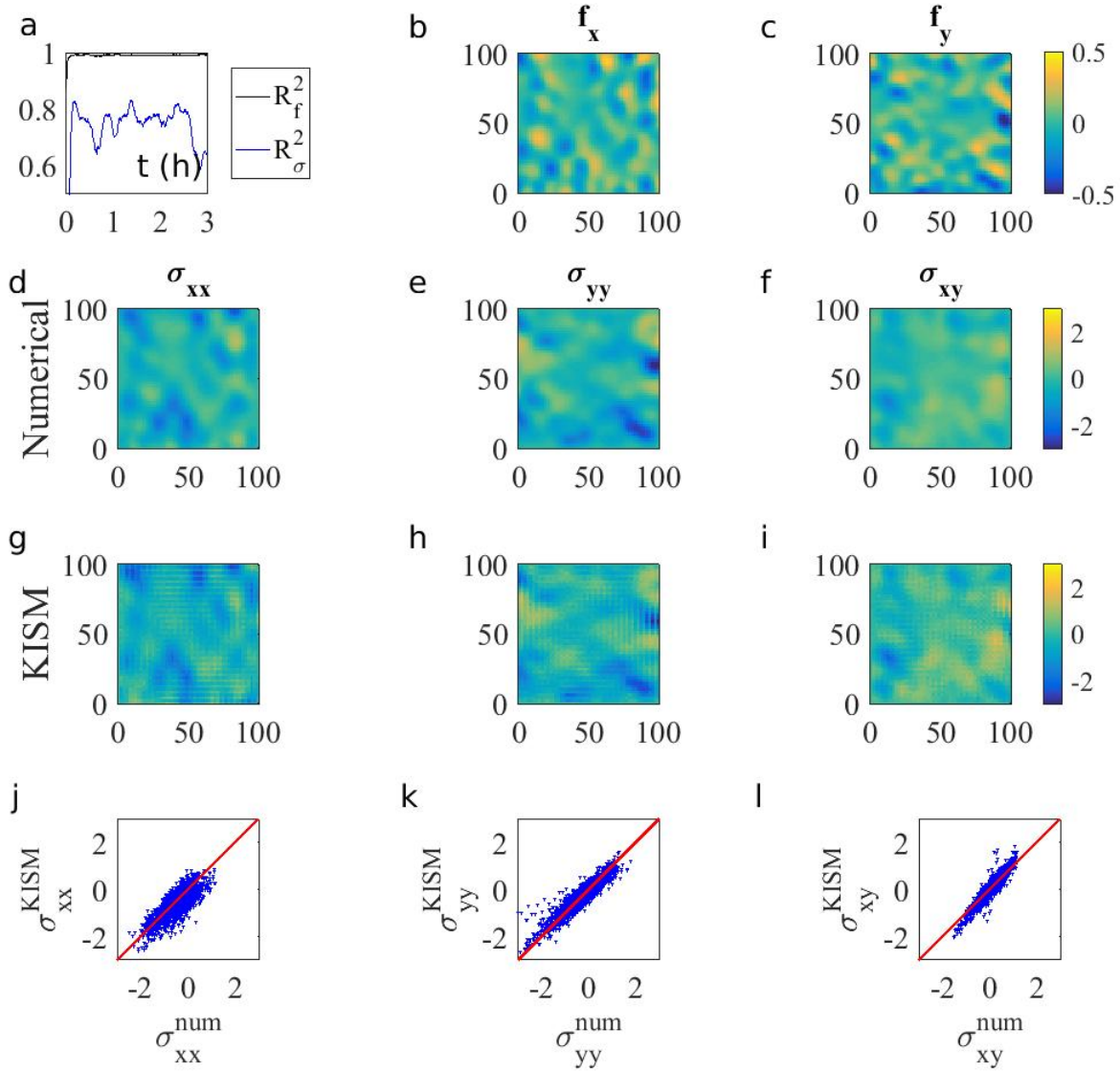


Figure 1: **Numerical validation.** (a)  $R_f^2$  and  $R_\sigma^2$  vs. time  $t$ . (b-c) Heat maps at  $t = 1$  h of the components  $f_x$  and  $f_y$  of the simulated traction force field  $\vec{f}^{\text{num}}$  (unit: kPa). Panels d-i: Heat maps at  $t = 1$  h of the components  $\sigma_{xx}$ ,  $\sigma_{yy}$  and  $\sigma_{xy}$  of: (d-f) the simulated stress field  $\sigma^{\text{num}}$ ; (g-i) the stress field  $\sigma^{\text{KISM}}$  inferred with KISM (unit: kPa  $\mu\text{m}$ ). Panels j-l: Comparison between inferred KISM stress  $\sigma^{\text{KISM}}$  and true simulated stress  $\sigma^{\text{num}}$ . The red line is the bisector  $y = x$ . The relative noise amplitude is  $s_{\text{exp}}^{\%} = 10\%$ . Time unit: h; length unit:  $\mu\text{m}$ .

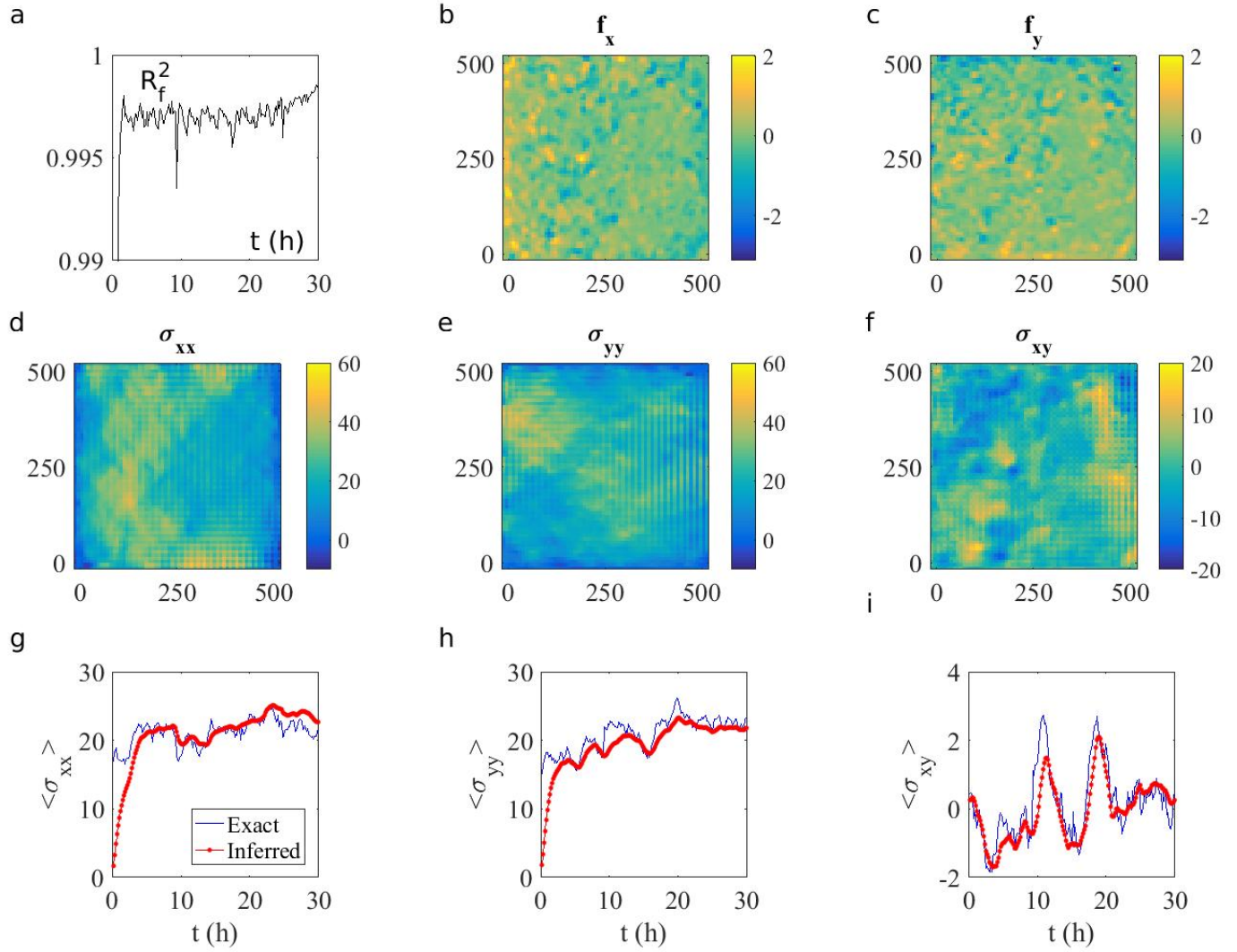


Figure 2: **Epithelial stress field: HaCaT cells.** (a) Coefficient of determination  $R_f^2$  vs. time  $t$ . (b-c) Heat maps of the components  $f_x$  and  $f_y$  of the experimental traction force field at  $t = 17$  h (unit: kPa). (d-f) Heat maps of the components  $\sigma_{xx}$ ,  $\sigma_{yy}$  and  $\sigma_{xy}$  of the stress field inferred with KISM at  $t = 17$  h (unit: kPa  $\mu\text{m}$ ). (g-i) Spatially-averaged stress components vs. time  $t$ . Blue line: exact values computed from the first moment of the traction force field,  $\langle \sigma_{ij} \rangle = -\langle f_i x_j \rangle$ . Red dots: values estimated by KISM. Globally ( $N = 8$ ), the average inferred pressure was negative,  $\langle \langle \pi \rangle \rangle^{\text{HaCaT}} = -23.9 \pm 2.4$  kPa  $\mu\text{m}$  between  $t = 10$ h and  $t = 30$ h, while the average inferred shear stress was  $\langle \langle \sigma_{xy} \rangle \rangle^{\text{HaCaT}} = 0.2 \pm 0.8$  kPa  $\mu\text{m}$  in the presence of sustained oscillations<sup>25</sup>. Time unit: h; length unit:  $\mu\text{m}$ .

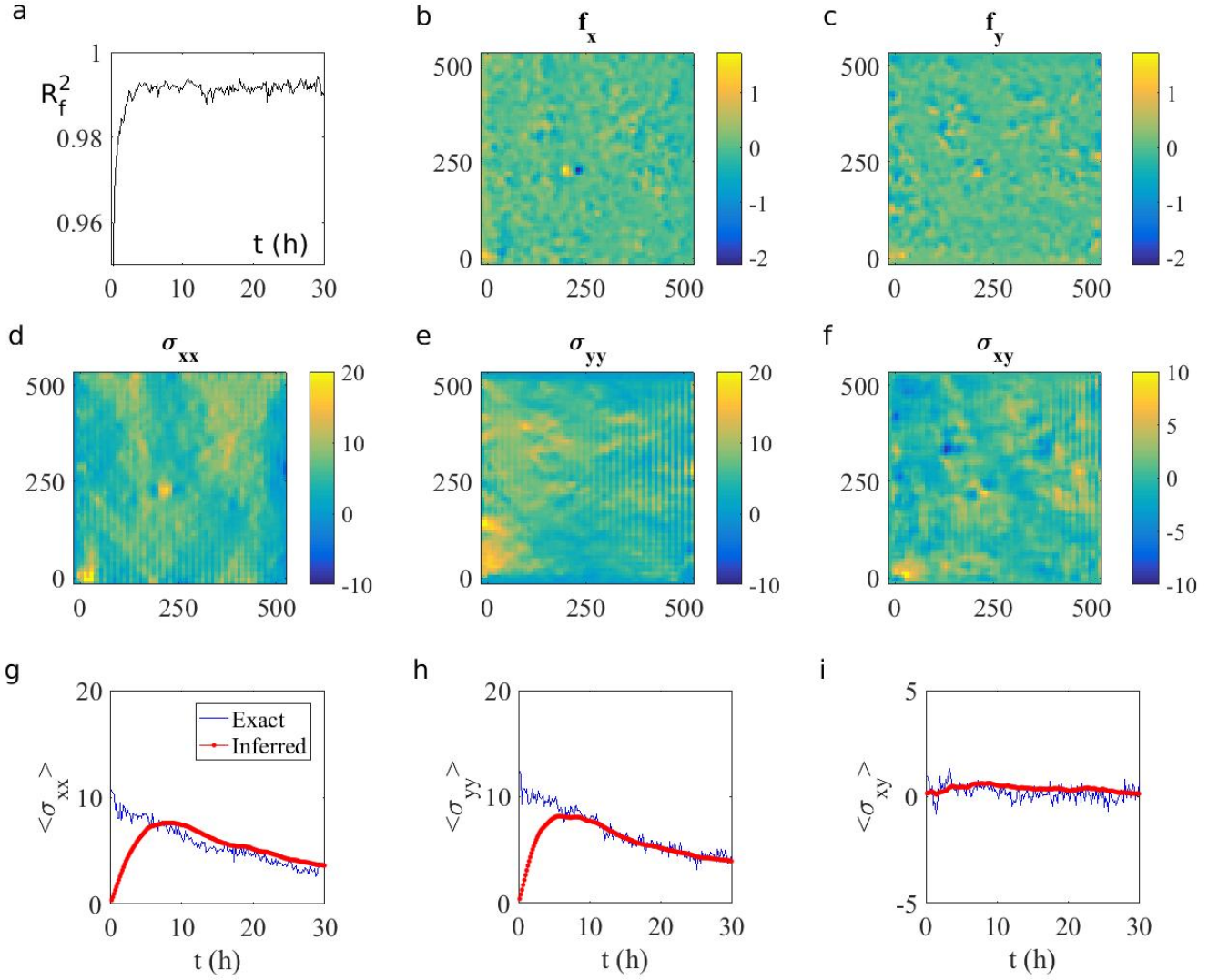


Figure 3: **Epithelial stress field: MDCK cells.** (a) Coefficient of determination  $R_f^2$  vs. time  $t$ . (b-c) Heat maps of the components  $f_x$  and  $f_y$  of the experimental traction force field at  $t = 17$  h (unit: kPa). (d-f) Heat maps of the components  $\sigma_{xx}$ ,  $\sigma_{yy}$  and  $\sigma_{xy}$  of the stress field  $\sigma^{\text{inf}}$  inferred with KISM at  $t = 17$  h (unit: kPa  $\mu\text{m}$ ). (g-i) Spatially-averaged stress components vs. time  $t$ . Blue line: exact values computed from the first moment of the traction force field,  $\langle \sigma_{ij} \rangle = -\langle f_i x_j \rangle$ . Red dots: values estimated by KISM. Globally ( $N = 5$ ), the average inferred pressure was negative between  $t = 10$  h and  $t = 30$  h,  $\langle \langle \pi \rangle \rangle^{\text{MDCK}} = -6.3 \pm 0.6$  kPa  $\mu\text{m}$ , while the average inferred shear stress was consistent with 0:  $\langle \langle \sigma_{xy} \rangle \rangle^{\text{MDCK}} = 0.2 \pm 0.2$  kPa  $\mu\text{m}$ . Time unit: h; length unit:  $\mu\text{m}$ .

We first validated KISM using traction force and stress data obtained by the numerical resolution of a simple model of a cellular sheet as a compressible, viscous material driven by active, motile force dipoles (Materials and methods, Numerical simulations and Movies S1-2). As shown in Fig. 1 when the relative noise amplitude was  $s_{\text{exp}}^{\%} = 10\%$ , our statistical model allowed to estimate accurately the simulated stress, with coefficients of determination  $R_f^2 \simeq 0.99$  and  $R_\sigma^2 \simeq 0.75$ . We checked that the accuracy of inference was insensitive to parameter values of the model, such as the correlation time  $\tau_d$  and noise amplitude  $s_v$  that control the time evolution of force dipoles. After a relaxation regime, typically shorter than ten frames, the dynamical rule (7-9) converged towards an accurate estimate of the stress field (Fig. 1). As expected from the asymptotic stability properties of Kalman filters<sup>17</sup>, the dynamics converged rapidly towards the same asymptotic state when we modified the initial condition as  $\hat{\sigma}^1 = c\gamma$  and  $S^1 = c^2\gamma^2 I$ ,  $c = 10^{-3}$  and  $c = 10^3$  (Figs. S1ab). The L2-norm  $\|K^t\|$  of the Kalman gain matrix also converged rapidly towards its asymptotic value in the same conditions, although on a slightly slower time scale (Fig. S1b). Varying the values of the noise variances  $\gamma^2$ , we observed that  $R_\sigma^2$  exhibited a shallow optimum close to the estimate  $\gamma^2 \approx 10^{-1} \text{Pa}^2 \mu\text{m}^2$  (Fig. S1c). Finally, we verified that the accuracy of inference was a decreasing function of  $s_{\text{exp}}^{\%}$  (Fig. S1d). Unsurprisingly, we observed that the accuracy of inference is a decreasing function of the time resolution (Fig. S1e), as well as of the scale over which the data may be coarse-grained (Fig. S1f).

From experimental traction force timelapse movies, we inferred the stress field of monolayers of human keratinocytes (HaCaT cells, Fig. 2, Movies S3-S5) and of Madin-Darby canine kidney cells (MDCK, Fig. 3, Movies S7-S9), see Materials and methods, Experimental methods. We considered the first 30 hours after confluence, during which sustained collective motion was observed (Movies S3 and S7) and ignored the jammed state arising later due to an increase in cell density. The accuracy of stress inference was quantified by the coefficient of determination  $R_f^2$  that compares the experimental traction force data with an “inferred” traction force field computed as the divergence of the inferred stress field. The value of  $R_f^2$  was always larger than 0.98 after a brief relaxation regime (Figs. 2a and 3a). Comparing the spatially-averaged stress values to their expected values (Materials and methods, Measures of accuracy), we also confirmed that the absolute value of the stress field was correctly estimated (Figs. 2g-i and 3g-i). Following Kalman filtering, the average inferred values are smoother than the true behavior. However, the stress computed at early time points may be highly inaccurate. We note that the relaxation time towards an accurate inference (a few hours) is similar for  $R_f^2$  and  $\langle \sigma_{ij} \rangle$ . As expected, both cell sheets were under tension (negative average pressure  $\pi = -(\sigma_{xx} + \sigma_{yy})/2$ ).

In order to characterize mechanical behavior at the scale of the tissue, all fields were coarse-grained over a mesoscopic scale  $\lambda = 25 \mu\text{m}$ . Motivated by previous work on epithelial rheology<sup>13,29</sup>, we focused on the cell shape tensor  $Q$  and the symmetrized velocity gradient tensor  $D$  (Materials and methods, Data analysis). Surprisingly, neither the stress tensor nor its time derivative were significantly correlated with  $D$  (Tables 1,2). Since the measured cell-shape (nematic) tensor  $Q$  was traceless, we focused on the deviatoric stress tensor,  $\text{dev } \sigma$ , which exhibited strong positive correlations with  $Q$  (Figs. 4ab-ef). A linear

	(dev $\sigma$ , $Q$ )	(dev $\sigma$ , dev $D$ )	(dev $\sigma$ , dev $\dot{\sigma}$ )	(dev $\sigma$ , $\dot{Q}$ )	(dev $\dot{\sigma}$ , dev $D$ )
HaCaT	$0.59 \pm 0.06$	$0.01 \pm 0.09$	$-0.01 \pm 0.02$	$-0.11 \pm 0.04$	$-0.01 \pm 0.07$
MDCK	$0.43 \pm 0.03$	$-0.02 \pm 0.04$	$-0.07 \pm 0.03$	$-0.13 \pm 0.02$	$0.01 \pm 0.02$

Table 1: **Correlation coefficients: deviators of tensors.**

HaCaT cells:  $N = 8$ ; MDCK cells:  $N = 5$ .

	(tr $\sigma$ , tr $D$ )	(tr $\sigma$ , tr $\dot{\sigma}$ )	(tr $\dot{\sigma}$ , tr $D$ )
HaCaT	$0.01 \pm 0.09$	$-0.01 \pm 0.03$	$0.01 \pm 0.09$
MDCK	$-0.03 \pm 0.05$	$-0.07 \pm 0.11$	$-0.02 \pm 0.01$

Table 2: **Correlation coefficients: traces of tensors.**

HaCaT cells:  $N = 8$ ; MDCK cells:  $N = 5$ .

regression of our data with the constitutive equation:  $\text{dev } \sigma = \zeta Q$  allowed to measure the material parameters  $\zeta^{\text{HaCaT}} = 26.0 \pm 0.3 \text{ kPa } \mu\text{m}$  ( $N = 8$ ) and  $\zeta^{\text{MDCK}} = 6.2 \pm 0.7 \text{ kPa } \mu\text{m}$  ( $N = 5$ ). Importantly, linear regressions for the two components of the deviatoric tensors yielded consistent slopes, in agreement with tensor symmetry. Elastic stress in epithelia is expected to be proportional to the cell shape tensor<sup>29</sup>. In addition, symmetries allow an active contribution to the same relationship, with an active parameter  $\zeta_a$ . We may thus define an effective shear elastic modulus  $G$  from the relation  $\zeta = G - \zeta_a$ , with  $\zeta_a > 0$  for extensile active materials such as an MDCK monolayer<sup>13</sup>. Although estimating  $G$  is here impractical, we note that the order of magnitude found for  $\zeta$  is compatible with estimates of elastic moduli derived from the force-extension curve of suspended cell monolayers<sup>30</sup>. In our data, the presence of dissipative behavior was suggested by correlations between dev  $\sigma$  and the time derivatives dev  $\dot{\sigma}$  and  $\dot{Q}$  (Table 1), where the dot denotes a total derivative. However, these correlations were typically smaller than 0.15, confirming that deviatoric stress depended dominantly on cell shape. Rheological behavior of the epithelial cell sheets was, to first order, that of an active and elastic material.

Finally, the measured stress field allowed to characterize plithotactic behaviour, defined as the tendency of cells to align their velocity with the principal axis of the tissue stress tensor during collective cell migration<sup>10</sup>. To quantify this tendency, we measured the angle  $\theta_{\sigma v}$  between the tissue velocity and the principal axis of the stress tensor. For MDCK cells, its pdf could be fitted by a zero-mean von Mises distribution of parameter  $\kappa_{\sigma v}^{\text{MDCK}} = 0.39 \pm 0.12$  (Fig. 4g). However, HaCaT cells did not exhibit plithotactic behaviour as the distribution of  $\theta_{\sigma v}$  was nearly uniform (Fig. 4c). Plithotactic behaviour, which may be related to cell-cell junction and cytoskeleton remodelling, was cell-type dependent<sup>10</sup>. For both cell types, the distribution of the angle  $\theta_{\sigma Q}$  between the principal axes of the stress and cell shape tensors was strongly peaked close to 0, and could be fitted by a zero-mean von Mises distribution with parameters  $\kappa_{\sigma Q}^{\text{HaCaT}} = 2.46 \pm 0.43$  and  $\kappa_{\sigma Q}^{\text{MDCK}} = 1.27 \pm 0.16$ . The cell shape tensor had an orientation close to that of the stress tensor (Figs. 4d 4h, Movies S6 and S10).

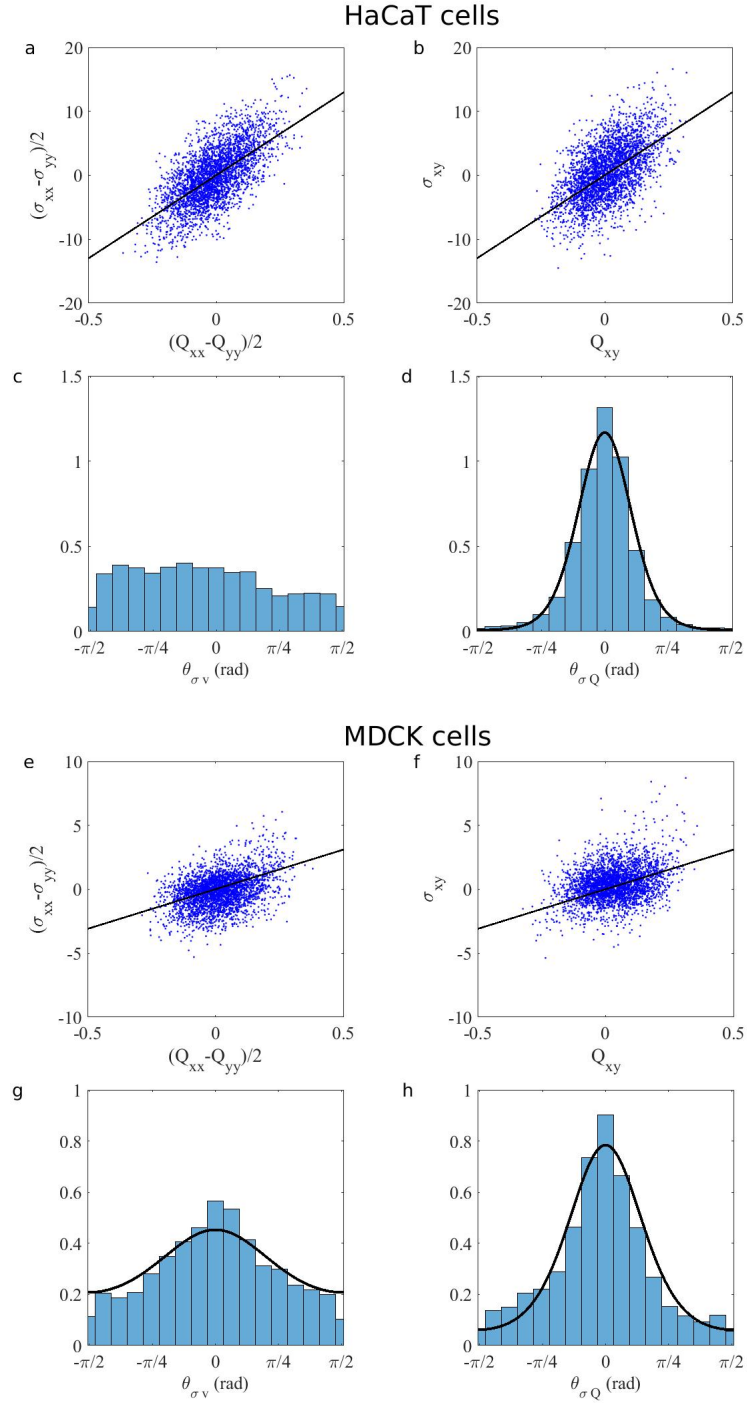


Figure 4: **Epithelial rheology. (a-d) HaCaT cells.** (a-b) Components of the deviatoric stress tensor (unit:  $\text{kPa } \mu\text{m}$ ) *vs.* same components of the cell shape tensor. The slope of the black lines is the average parameter value  $\zeta = 26.0 \text{ kPa } \mu\text{m}$  ( $N = 8$ ). (c-d) Pdfs of the angles  $\theta_{\sigma v}$  and  $\theta_{\sigma Q}$ , given a stress anisotropy belonging to its highest quintile. The black curve is a zero-mean von Mises distribution with the average parameter value  $\kappa_{\sigma Q} = 2.46$  ( $N = 8$ ). **(e-h) MDCK cells.** Same representations as for HaCaT cells, with parameter values  $\zeta = 6.2 \text{ kPa } \mu\text{m}$ ,  $\kappa_{\sigma v} = 0.39$ ,  $\kappa_{\sigma Q} = 1.27$  ( $N = 5$ ).

## Discussion

To summarize, Kalman filtering led to accurate estimates of epithelial stress, without any assumption on tissue mechanical properties. We expect that its applicability and reliability would not differ in the case of time-dependent<sup>31</sup>, or spatially inhomogeneous<sup>32</sup> rheological properties. The only assumption underlying KISM, that the observation and evolution noises are Gaussian processes, could be relaxed using particle filtering, where arbitrary pdfs are sampled by Markov chain Monte Carlo methods. We opted for the simpler, Gaussian case given the accuracy of estimates thus obtained. Note that a spatial prior may be used when Kalman filtering<sup>16</sup>, closely following Bayesian inversion stress microscopy: in fact BISM may even be used to set the initial condition<sup>14</sup>. A drawback is the need to introduce a dimensionless regularisation parameter  $\Lambda$ , whose value must be determined from data<sup>33</sup>. We opt here for simplicity, and propose an inference method that does not require prior information, and therefore does not explicitly regularize the solution. Note that KISM estimates are generally in good agreement with BISM estimates (Fig. S4). However KISM cannot be applied to single images, by construction, and its accuracy decreases with the time resolution of the traction force movie. Otherwise, the conditions for applicability of KISM are the same as for BISM, since the two inference methods share the same physical constraints. Although the cell sheet should in principle be flat, and be characterized by an approximately constant height  $h(\vec{r}, t)$  for a description in terms of two-dimensional stress to be valid, this last assumption may be relaxed, as KISM may be implemented by replacing the traction force  $f$  by the ratio  $\vec{f}(\vec{r}, t)/h(\vec{r}, t)$  and inferring the three-dimensional stress  $\sigma_{3D} = \sigma/h$  from  $\text{div } \sigma_{3D} = \vec{f}/h$  as above.

In principle, Kalman smoothing<sup>16,34</sup> may further improve the accuracy of inference, as information contained in frames posterior to that of the current estimate is also taken into account, in addition to the forward evolution in time. We implemented a Kalman, fixed-interval smoother for stress inference, but found that the improvement compared to the Kalman filter was marginal, except for the first time steps<sup>33</sup>, where the accuracy of Kalman filtering is limited. Since the additional computational cost required by smoothing is substantial, mostly in terms of memory allocation, we also opt for simplicity concerning this aspect, and favor Kalman filtering, rather than Kalman smoothing for stress estimation.

A geometry-based Bayesian inversion method has been developed to infer the stress field of flat epithelial cell sheets *in vivo*, for instance in the *Drosophila* pupa, using the positions of cell vertices and orientations of cell junctions as input data<sup>7,35</sup>. We believe that Kalman filtering could also be applied to geometry-based inference so as to dispense with the need of a prior.

Remarkably, cell shape anisotropy was a good, zero-th order proxy for deviatoric stress, up to a cell type-dependent scale parameter  $\zeta$  that we measured. This observation is consistent with the model proposed by some of us<sup>29</sup> in the limit of an active and elastic rheology, provided that cell rearrangements are rare. This result, obtained here for deviatoric stress in 2D, is reminiscent of that obtained for 1D stress in expanding MDCK monolayers<sup>36</sup>. Of note, the active viscous model shown in<sup>31</sup> to explain quantitatively epithelial cell monolayer expansion can also be interpreted as an elastic and active model

in this quasi-1D geometry.

The evolution equation (6) may be made more complex than a random walk to test the relevance of a given rheological model. Recent work<sup>37</sup> combined a Rauch-Tung-Striebel smoother with an Expectation-Maximization algorithm to infer the elastic moduli of an expanding cell monolayer, found in the kPa  $\mu\text{m}$  range. However, a natural extension of the approach to Maxwell's model of a viscoelastic liquid led to overfitting and failed to yield estimates of monolayer viscosities. Both results are consistent with our observations.

Epithelial rheology could be quantified in physiological conditions, where the ranges of forces and of deformations are not determined by an external operator, but by the spontaneous activity of the cells. The HaCaT cell sheet was likely stiffer than the MDCK cell sheet: Determining the molecular cause of this difference is an open question that we would like to address in the future. This work paves the way towards the inference of the constitutive equations of *in vitro* cellular sheets from experimental data.

## Acknowledgements

Financial supports from the European Research Council under the European Union's Seventh Framework Programme (FP7/2007-2013) / ERC grant agreement 617233 (BL), the LABEX "Who am I?", and the Agence National de la Recherche (POLCAM, ANR-17-CE13-0013) are gratefully acknowledged.

## REFERENCES

- [1] Heisenberg, C.-P., and Y. Bellaïche, 2013. Forces in tissue morphogenesis and patterning. *Cell* 153:948–962.
- [2] Iskratsch, T., et al., 2014. Appreciating force and shape - the rise of mechanotransduction in cell biology. *Nat Rev Mol Cell Biol* 15:825–833.
- [3] Vining, K. H., and D. J. Mooney, 2017. Mechanical forces direct stem cell behaviour in development and regeneration. *Nat Rev Mol Cell Biol* 18:728–742.
- [4] Ladoux, B., et al., 2015. The mechanotransduction machinery at work at adherens junctions. *Integr Biol* 7:1109–1119.
- [5] Sugimura, K., et al., 2016. Measuring forces and stresses in situ in living tissues. *Development* 143:186–196.
- [6] Bonnet, I., et al., 2012. Mechanical state, material properties and continuous description of an epithelial tissue. *J Roy Soc Interface* 9:2614–2623.
- [7] Ishihara, S., and K. Sugimura, 2012. Bayesian inference of force dynamics during morphogenesis. *J Theor Biol* 313:201–211.
- [8] Style, R. W., et al., 2014. Traction force microscopy in physics and biology. *Soft Matter* 10:4047–4055.

- [9] Schwarz, U., and J. Soiné, 2015. Traction force microscopy on soft elastic substrates: A guide to recent computational advances. *BBA - Mol Cell Res* 1853:3095–3104.
- [10] Tambe, D., et al., 2011. Collective cell guidance by cooperative intercellular forces. *Nat Mater* 10:469–475.
- [11] Guevorkian, K., et al., 2010. Aspiration of biological viscoelastic drops. *Phys Rev Lett* 104:218101.
- [12] Marmottant, P., et al., 2009. The role of fluctuations and stress on the effective viscosity of cell aggregates. *Proc Natl Acad Sci U S A* 106:17271–17275.
- [13] Saw, T. B., et al., 2017. Topological defects in epithelia govern cell death and extrusion. *Nature* 544:212–216.
- [14] Nier, V., et al., 2016. Inference of internal stress in a cell monolayer. *Biophys J* 110:1625–1635.
- [15] Kalman, R. E., 1960. A new approach to linear filtering and prediction problems. *J Basic Eng* 82:35–45.
- [16] Kaipio, J., and E. Somersalo, 2006. Statistical and computational inverse problems. Springer.
- [17] Anderson, B., and J. Moore, 1979. Optimal filtering. Prentice Hall.
- [18] Faragher, R., 2012. Understanding the Basis of the Kalman Filter Via a Simple and Intuitive Derivation [Lecture Notes]. *IEEE Signal Processing Magazine* 29:128–132.
- [19] Landau, L., and E. Lifshitz, 1975. Elasticity theory. Pergamon Press.
- [20] du Roure, O., et al., 2005. Force mapping in epithelial cell migration. *Proc Natl Acad Sci U S A* 102:2390–2395.
- [21] Sepúlveda, N., et al., 2013. Collective cell motion in an epithelial sheet can be quantitatively described by a stochastic interacting particle model. *PLoS Comput Biol* 9:e1002944.
- [22] Hecht, F., 2012. New development in FreeFem++. *J Num Math* 20:251–266.
- [23] Murphy, K., 2012. Machine Learning - A Probabilistic Perspective. MIT press.
- [24] Vedula, S. R. K., et al., 2014. Microfabricated environments to study collective cell behaviors. *Methods Cell Biol* 120:235–252.
- [25] Peyret, G., 2016. Influence des contraintes géométriques sur le comportement collectif de cellules épithéliales. Ph.D. thesis, Université Paris Diderot, Paris, France.
- [26] Martiel, J.-L., et al., 2015. Measurement of cell traction forces with ImageJ. *Methods Cell Biol* 125:269–287.

- [27] Rezakhaniha, R., et al., 2012. Experimental Investigation of Collagen Waviness and Orientation in the Arterial Adventitia Using Confocal Laser Scanning Microscopy. *Biomech Model Mechanobiol* 11:461–473.
- [28] Fisher, N., 1995. Statistical analysis of circular data. Cambridge University Press.
- [29] Ishihara, S., et al., 2017. From cells to tissue: A continuum model of epithelial mechanics. *Phys Rev E* 96:022418.
- [30] Harris, A. R., et al., 2012. Characterizing the mechanics of cultured cell monolayers. *Proc Natl Acad Sci U S A* 109:16449–16454.
- [31] Blanch-Mercader, C., et al., 2017. Effective viscosity and dynamics of spreading epithelia: a solvable model. *Soft Matter* 13:1235–1243.
- [32] Rodríguez-Franco, et al., 2017. Long-lived force patterns and deformation waves at repulsive epithelial boundaries. *Nature Materials* 16:1029–1037.
- [33] Nier, V., 2016. Estimation statistique des propriétés physiques de monocouches cellulaires. Ph.D. thesis, Université Pierre et Marie Curie, Paris, France.
- [34] Särkkä, S., 2013. Bayesian filtering and smoothing. Cambridge University Press.
- [35] Ishihara, S., et al., 2013. Comparative study of non-invasive force and stress inference methods in tissue. *Eur Phys J E* 36:9859.
- [36] Vincent, R., et al., 2015. Active tensile modulus of an epithelial monolayer. *Phys Rev Lett* 115:248103.
- [37] Kondo, Y., et al., 2018. Inverse tissue mechanics of cell monolayer expansion. *PLOS Computational Biology* 14:e1006029.

# Supporting Material

## Movies

- Movie S1. Numerical simulation: traction force,  $x$  and  $y$  components. Length unit:  $\mu\text{m}$ . Force unit: kPa. Time resolution:  $\Delta t = 30$  s. Spatial resolution:  $\Delta x = 2 \mu\text{m}$ . Duration: 3 h.
- Movie S2. Numerical simulation: stress,  $xx$ ,  $yy$  and  $xy$  components. Length unit:  $\mu\text{m}$ . Stress unit: kPa  $\mu\text{m}$ . Time resolution:  $\Delta t = 30$  s. Spatial resolution:  $\Delta x = 2 \mu\text{m}$ . Duration: 3 h.
- Movie S3. Experimental data: HaCaT cells. Scale bar:  $100 \mu\text{m}$ .
- Movie S4. Experimental data: HaCaT cells, traction force,  $x$  and  $y$  components. Length unit:  $\mu\text{m}$ . Force unit: kPa. Time resolution:  $\Delta t = 10$  min. Spatial resolution:  $\Delta x = 3.9 \mu\text{m}$ . Duration: 20 h.
- Movie S5. Inferred data: HaCaT cells, stress,  $xx$ ,  $yy$  and  $xy$  components. Length unit:  $\mu\text{m}$ . Stress unit: kPa  $\mu\text{m}$ . Time resolution:  $\Delta t = 10$  min. Spatial resolution:  $\Delta x = 3.9 \mu\text{m}$ . Duration: 20 h.
- Movie S6. Rheology: HaCaT cells. Left: velocity; center: principal axis of the deviatoric stress tensor  $\text{dev } \sigma$ ; right: principal axis of the cell shape tensor  $Q$  (arbitrary units). Time resolution:  $\Delta t = 10$  min. Spatial resolution:  $\lambda = 25 \mu\text{m}$ . Duration: 20 h.
- Movie S7. Experimental data: MDCK cells. Scale bar:  $100 \mu\text{m}$ .
- Movie S8. Experimental data: MDCK cells, traction force,  $x$  and  $y$  components. Length unit:  $\mu\text{m}$ . Force unit: kPa. Time resolution:  $\Delta t = 10$  min. Spatial resolution:  $\Delta x = 3.9 \mu\text{m}$ . Duration: 20 h.
- Movie S9. Inferred data: MDCK cells, stress,  $xx$ ,  $yy$  and  $xy$  components. Length unit:  $\mu\text{m}$ . Stress unit: kPa  $\mu\text{m}$ . Time resolution:  $\Delta t = 10$  min. Spatial resolution:  $\Delta x = 3.9 \mu\text{m}$ . Duration: 20 h.
- Movie S10. Rheology, MDCK cells. Left: velocity; center: principal axis of the deviatoric stress tensor  $\text{dev } \sigma$ ; right: principal axis of the cell shape tensor  $Q$  (arbitrary units). Time resolution:  $\Delta t = 10$  min. Spatial resolution:  $\lambda = 25 \mu\text{m}$ . Duration: 20 h.

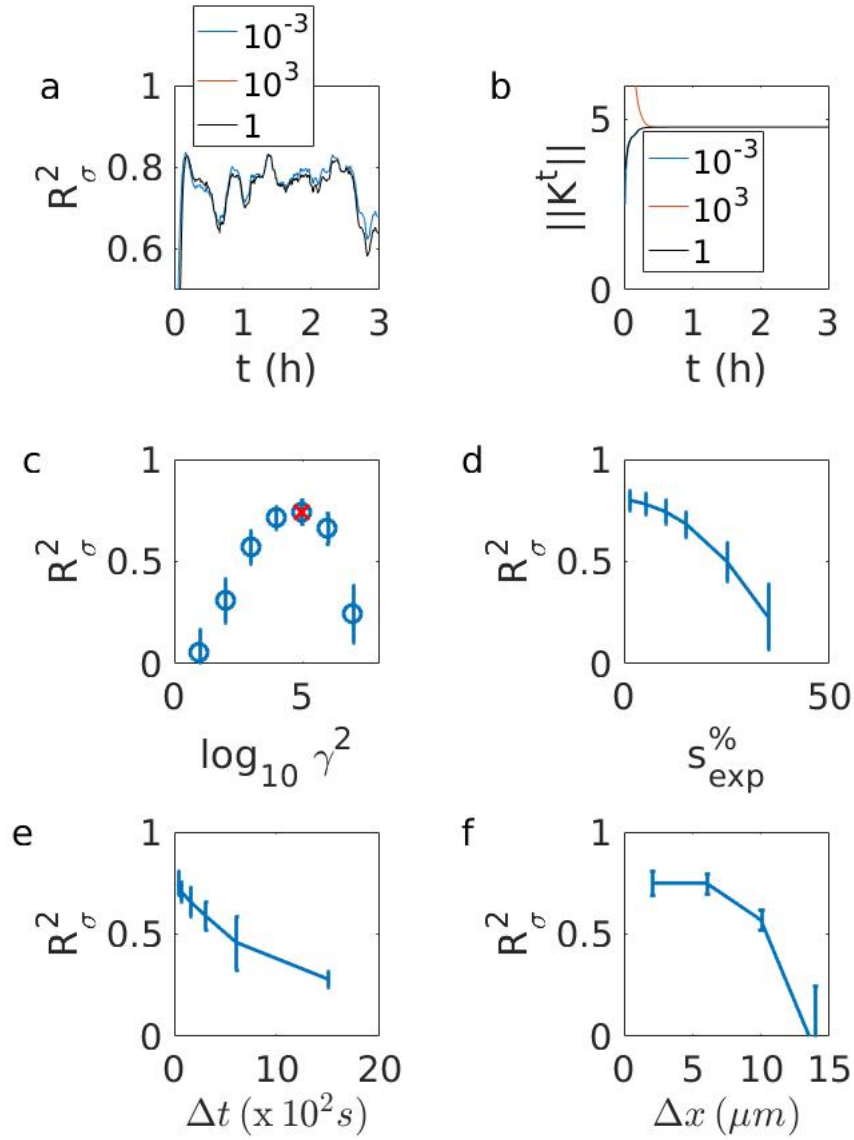


Figure S1: **Robustness.** (a-b)  $R_\sigma^2$  and  $\|K^t\|$  vs. time  $t$  (unit: h) for initial conditions differing by a multiplicative factor  $c = 10^{-3}, 1, 10^3$ . The case  $c = 1$  corresponds to the inference performed as in Fig. 1, and is used in other panels of this figure. (c)  $R_\sigma^2$  vs.  $\gamma^2$ . The maximum of  $R_\sigma^2$  is close to the estimated value  $\gamma^2 = 9.2 \cdot 10^4 \text{ Pa}^2 \mu\text{m}^2$  (red cross) set as described in the Materials and methods, and used in other panels of this figure. (d)  $R_\sigma^2$  vs.  $s_{\text{exp}}^{\%}$ . The noise level in other panels is  $s_{\text{exp}}^{\%} = 10\%$ . (e)  $R_\sigma^2$  vs. time resolution  $\Delta t$ . The time resolution in other panels is  $\Delta t = 30$  s. (f)  $R_\sigma^2$  vs. spatial resolution  $\Delta x$ . The spatial resolution in other panels is  $\Delta x = 2 \mu\text{m}$ .

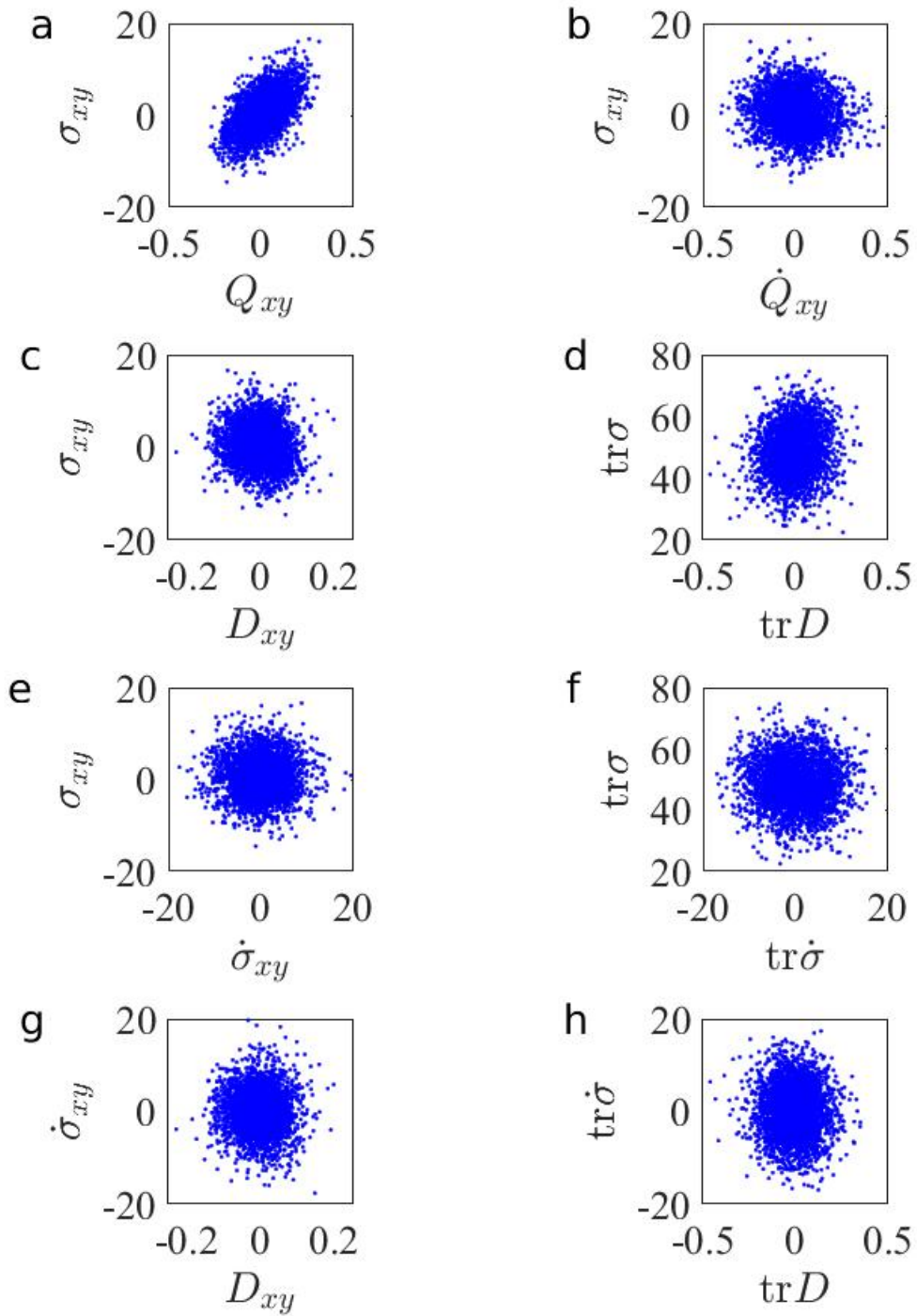


Figure S2: **Scatter plots: HaCaT cells. Shear component and trace.** **a**  $\sigma_{xy}$  vs.  $Q_{xy}$ ; **b**  $\sigma_{xy}$  vs.  $\dot{Q}_{xy}$ ; **c**  $\sigma_{xy}$  vs.  $D_{xy}$ ; **d**  $\text{tr}\sigma$  vs.  $\text{tr}D$ ; **e**  $\sigma_{xy}$  vs.  $\dot{\sigma}_{xy}$ ; **f**  $\text{tr}\sigma$  vs.  $\text{tr}\dot{\sigma}$ ; **g**  $\dot{\sigma}_{xy}$  vs.  $D_{xy}$ ; **h**  $\text{tr}\dot{\sigma}$  vs.  $\text{tr}D$ ; Stress unit:  $\text{kPa}\mu\text{m}$ . Time unit: h. Velocity gradient unit:  $\text{h}^{-1}$ . Same data as in Fig. 4. The average correlation coefficients are given in Tables 1 and 2 ( $N = 8$ ).

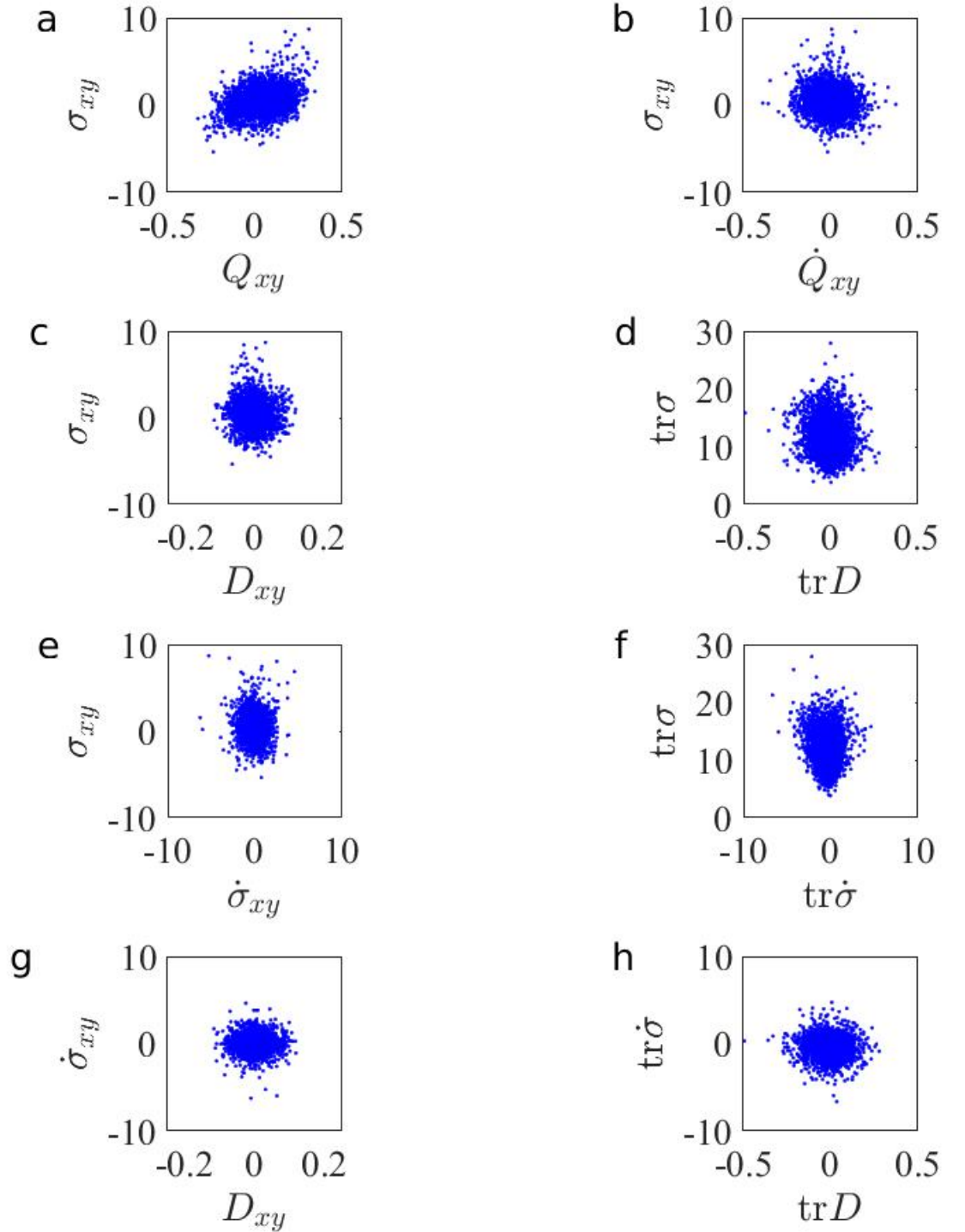


Figure S3: **Scatter plots: MDCK cells. Shear component and trace.** **a**  $\sigma_{xy}$  vs.  $\dot{Q}_{xy}$ ; **b**  $\sigma_{xy}$  vs.  $\dot{Q}_{xy}$ ; **c**  $\sigma_{xy}$  vs.  $D_{xy}$ ; **d**  $\text{tr} \sigma$  vs.  $\text{tr} D$ ; **e**  $\sigma_{xy}$  vs.  $\dot{\sigma}_{xy}$ ; **f**  $\text{tr} \sigma$  vs.  $\text{tr} \dot{\sigma}$ ; **g**  $\dot{\sigma}_{xy}$  vs.  $D_{xy}$ ; **h**  $\text{tr} \dot{\sigma}$  vs.  $\text{tr} D$ ; Stress unit:  $\text{kPa} \mu\text{m}$ . Time unit:  $\text{h}^{-1}$ . Same data as in Fig. 4. The correlation coefficients are given in Tables 1 and 2 ( $N = 5$ ).

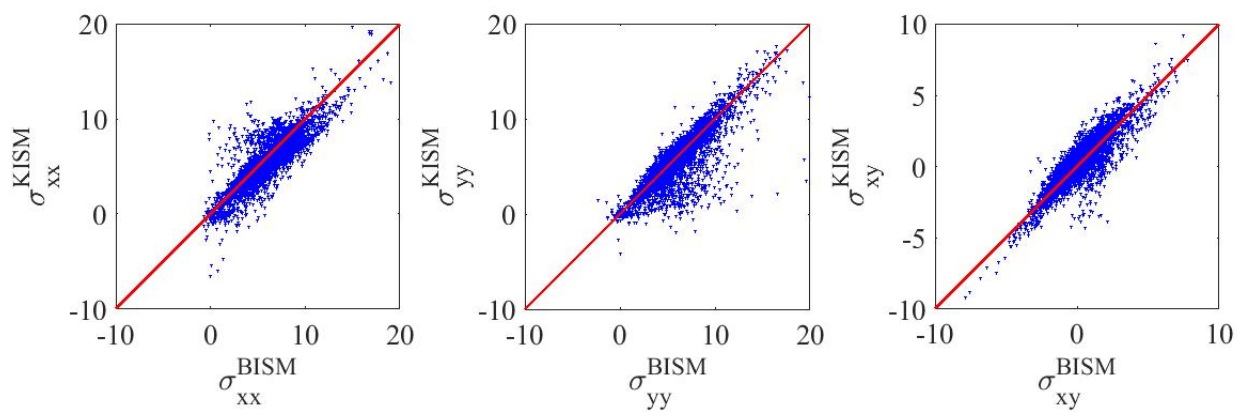


Figure S4: **Comparison with BISM.** Components of the KISM stress (as in Fig. 3, MDCK cells) *vs.* corresponding components of the BISM stress (regularisation parameter  $\Lambda = 10^{-6}$ ). The red lines are the bisectors  $y = x$ . Unit:  $\text{kPa } \mu\text{m}$ .